

1 **Development of a continuous UAV-mounted air sampler and** 2 **application to the quantification of CO₂ and CH₄ emissions from a** 3 **major coking plant**

4 Tianran Han¹, Conghui Xie¹, Yayong Liu¹, Yanrong Yang¹, Yuheng Zhang¹, Yufei Huang¹, Xiangyu
5 Gao², Xiaohua Zhang³, Fangmin Bao⁴, Shao-Meng Li¹

6 ¹ State Key Joint Laboratory of Environmental Simulation and Pollution Control, College of Environmental Sciences and
7 Engineering, Peking University, Beijing 100871, P.R. China

8 ² Beijing Wisdominc Technology Co., Ltd., Beijing, P.R. China

9 ³ Suzhou Environmental Monitoring Center, Jiangsu Province, P.R. China

10 ⁴ Jiangsu Shagang Group Co., Ltd., Beijing, P.R. China

11 *Correspondence to:* Shao-Meng Li (shaomeng.li@pku.edu.cn)

12 **Abstract.** The development in uncrewed aerial vehicle (UAV) technologies over the past decade has led to a plethora of
13 platforms that can potentially enable greenhouse gas emission quantification. Here, we report the development of a new
14 air sampler, consisting of a pumped stainless coiled tube of 150 m in length with controlled time-stamping, and its
15 deployment from an industrial UAV to quantify CO₂ and CH₄ emissions from the main coking plant stacks of a major
16 steel maker in eastern China. Laboratory tests show that the time series of CO₂ and CH₄ measured using the sampling
17 system is smoothed when compared to online measurement by the cavity ring-down spectrometer (CRDS) analyzer.
18 Further analyses show that the smoothing is akin to a convolution of the true time series signals with a heavy-tailed digital
19 filter. For field test, the air sampler was mounted on the UAV and flown virtual boxes around two stacks in the coking
20 plant at Shagang Steel Group. Mixing ratios of CO₂ and CH₄ in air and meteorological parameters were measured from
21 the UAV during the test flight. A mass-balance computational algorithm was used on the data to estimate the CO₂ and
22 CH₄ emission rates from the stacks. Using this algorithm, the emission rates for the two stacks from the coking plant were
23 calculated to be $0.12 \pm 0.014 \text{ t h}^{-1}$ for CH₄ and $110 \pm 18 \text{ t h}^{-1}$ for CO₂, the latter being in excellent agreement with material
24 balance based estimates. A Gaussian plume inversion approach was also used to derive the emission rates and the results
25 were compared with those derived using the mass-balance algorithm, showing a good agreement between the two methods.

26 **1 Introduction**

27 Atmospheric carbon dioxide (CO₂) and methane (CH₄) are the two major anthropogenic greenhouse gases (GHGs). Both
28 CO₂ and CH₄ in the atmosphere have been increasing since the industrial revolution, particularly rapidly over the past ten
29 years. Global networks consistently show that the globally averaged annual mean CO₂ molar fraction in the atmosphere
30 increased by 5.0% from 2011 to 2019, reaching 409.9 ± 0.4 ppm in 2019. Likewise, the globally averaged surface
31 atmospheric molar fraction of CH₄ in 2019 was 1866.3 ± 3.3 ppb, 3.5% higher than in 2011 (IPCC, 2021). CH₄ is a
32 stronger absorber of Earth's thermal infrared radiation than CO₂, with its global warming potential (GWP) 32 times
33 greater than that of CO₂ over a 100-year horizon (Saunois et al., 2020). Although its molar fractions in the atmosphere
34 are about 200 times lower than those of CO₂, the total radiative forcing of ~ 1.0 W m⁻² for CH₄ is about half of that of CO₂
35 (~ 2 W m⁻²) (IPCC, 2021), contributed by its direct radiative forcing of (0.6 ± 0.1) W m⁻² and indirect forcing of 0.4 W m⁻²
36 resulting from chemical reactions producing other GHGs including CO₂, O₃, and stratospheric water (Turner et al., 2019).
37 Furthermore, although global anthropogenic CH₄ emissions are estimated to be only 3% of the global anthropogenic CO₂
38 emissions in units of carbon mass flux, the increase in atmospheric CH₄ is responsible for about 20% of the warming
39 induced by long-lived greenhouse gases since pre-industrial times (Etminan et al., 2016). Both CO₂ and CH₄ are produced
40 and released into the atmosphere from a variety of natural and anthropogenic sources. Natural emission sources include
41 vegetation, oceans, volcanoes and naturally occurring wildfires, but most of the increases in atmospheric CO₂ and CH₄
42 are considered to have resulted from anthropogenic emissions, from sources including fossil fuel production and uses,
43 agricultural activities, land use and industrial processes (IPCC, 2021).

44 Quantification of CO₂ and CH₄ emissions from sources requires continuous measurements of their mixing ratios as
45 well as meteorological parameters using a variety of stationary and mobile platforms, including ground-based vehicles
46 (Rella et al., 2015; Brantley et al., 2014), towers (Helfter et al., 2016; Takano and Ueyama, 2021), aircrafts (Li et al.,
47 2017; Liggio et al., 2019) and satellites (Miller et al., 2013; Turner et al., 2015). Small uncrewed aerial vehicles (UAVs)
48 have become emerging platforms due to the recent rapid technological developments. They are flexible, versatile and
49 relatively inexpensive. Most importantly, a UAV platform fills the sampling space between the ground and altitudes of
50 up to hundreds of meters above ground, in which other mobile platforms have been unable to operate (Shaw et al., 2021).
51 Due to their relatively low flying speeds, UAV platforms offer a high spatiotemporal resolution for sampling and thus
52 enabling accurate plume mapping. On the other hand, UAVs have limited endurance, being constrained by battery
53 capacities and payloads, making them more suitable for small facility flux quantification.

54 UAV platforms have been used to quantify CH₄ emissions in several studies, mainly focused on facility-scale
55 emission sources including landfills (Allen et al., 2019; Bel Hadj Ali et al., 2020), coal mines (Andersen et al., 2021),
56 dairy farms (Vinkovic et al., 2022), wastewater treatment plants (Gålfalk et al., 2021) and oil and gas facilities (Golston
57 et al., 2018; Li et al., 2020; Nathan et al., 2015; Shah et al., 2020; Tuzson et al., 2021). UAV-based CH₄ measurements
58 are generally made with three different methods: collecting on-board samples for subsequent analysis, tethered sampling
59 to a sensor on the ground and on-line measurements (Shaw et al., 2021). Gas samples could be stored onboard a UAV for
60 subsequent analyses on the ground after landing, using air bags (Brownlow et al., 2016) or sampling canisters (Chang et
61 al., 2016). Andersen et al. developed a UAV-based active AirCoresystem, consisting of a long coiled stainless-steel tubing,
62 a small pinhole orifice, and a pump that drags air through the tube (Andersen et al., 2018), which allows for a higher
63 spatiotemporal resolution in the measurements. Direct comparisons between a quantum cascade laser absorption
64 spectrometer (QCLAS) and the active AirCore measurements show that the active AirCore measurements are smoothed
65 by 20 s and had an average time lag of 7 s. The active AirCore measurements also stretch linearly with time at an average
66 rate of 0.06 s for every second of QCLAS measurement (Morales et al., 2022). The advances in active AirCore sampling
67 have made UAV measurements for CH₄ emissions feasible, even if still with rooms for improvement. Studies of using
68 UAVs for CO₂ plume detection and mapping from anthropogenic sources have also been reported (Reuter et al., 2021;
69 Liu et al., 2022; Leitner et al., 2023; Chiba et al., 2019). Reuter et al. presented the development of a UAV platform to
70 quantify the CO₂ emissions of anthropogenic point sources by deployment of an NDIR (non-dispersive infrared) detector
71 and a 2-D ultrasonic acoustic resonance anemometer on the platform (Reuter et al., 2021).

72 In this study, we developed a new active air sampling system for deployment from a UAV on a trajectory in the
73 three-dimensional space to measure CO₂ and CH₄. The complete sampler plus UAV system was deployed to quantify
74 CO₂ and CH₄ emissions from the stacks of the main coking plant of Shagang, the largest private steel maker in China.
75 The top-down emission rate retrieval algorithm (TERRA) (Gordon et al., 2015) was applied to the UAV data to determine
76 stack CH₄ and CO₂ emissions rates. The iron and steel industry is one of the largest contributing industries to global GHG
77 emissions, accounting for around 7% of global total GHG emissions (Hasanbeigi, 2022). Coke production is one major
78 process of iron and steel making that generate emissions of CO₂ and CH₄. During coke production, coking coal is used to
79 manufacture metallurgical coke that is subsequently used as the reducing agent in the production of iron and steel (U.S.
80 Environmental Protection Agency, 2016). Coke oven gas is the main sources of CO₂ and CH₄ emissions during coke
81 production (Angeli et al., 2021; IPCC, 2006). China is the largest coke producer in the world, with a coke production of
82 4.72 billion tons in 2020. The GHG emissions from coke production in China are reported based on the Tier 1

83 methodology of IPCC Guidelines, which multiplies generic default emission factors with the tonnage of coke produced
84 (Ministry of Ecology and Environment of China, 2018). Tier 1 methodologies are the simplest and least complex requiring
85 less resources on collecting the necessary data and producing GHG emission estimates. The present UAV measurement-
86 based emission results can be compared with material balance based emission estimates and the emissions based on the
87 Tier 1 emission factors and coke production at the plant, and to shed light on the uncertainties related to Tier 1 emission
88 factors in the case of CH₄ emissions.

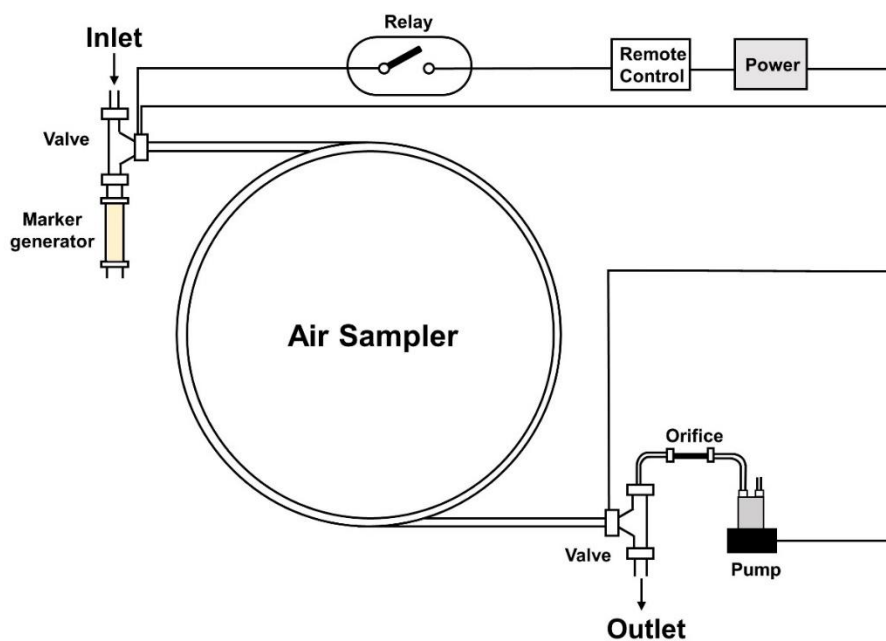
89 **2.Method**

90 **2.1 The air sampling system**

91 To realize GHG emission quantification by UAV measurement, a new compact air sampling system was developed based
92 on a variation of the active AirCore method. The AirCore system contains a 150-m-long stainless steel tube, open at one
93 end and closed at the other, that relies on positive changes in ambient pressure for passive sampling of the atmosphere
94 (Karion et al., 2010). Figure 1 shows an overview of the patented design for this sampler. It consists of a 150 m long thin-
95 walled 1/8 inch outside diameter stainless-steel tubing, a pump, a micro-orifice, a CO₂ marker generator, two three-way
96 solenoid valves and electric relays, with all electrical devices powered by a 12V battery. The tubing is wound into a
97 multilayer coil, in whose center the other components of the system are mounted. The system is housed in the highly
98 compact patented carbon fiber assembly design of 280 mm diameter and 98 mm height, that can be quickly mounted at
99 and dismantled from the bottom of an UAV. The sampler weighs about 5.9 kg and allows for continuous sampling up to
100 35 minutes.

101 The sampler air intake is mounted at 70 cm above the center of gravity of the UAV, placed nearby a sonic
102 anemometer (below) for ensuring sampling the same air mass where wind speed is measured. The time stamp of the
103 mixing ratio observation was corrected for the short time lag of 4 seconds between sampling at the air intake and the thin-
104 walled stainless-steel tubing attributable to the length of the Teflon inlet tube. Shortly before every flight, the pump is
105 remotely turned on to sample the CO₂ marker for 5 seconds and then to collect air samples. The CO₂ markers help to
106 identify the starting point and specific times subsequently during the UAV air sampling in data extraction and analysis.
107 During flight, the pump would alternatively sample the marker and the ambient air on a preset timing schedule. The
108 sampling flow rate remains at 18 ccm during the entire flight, controlled with the micro-orifice which is placed between
109 the pump and the coiled tubing. After landing, the pump is remotely turned off and the air sample in the sampling tubing

110 is immediately analyzed with a cavity ring-down spectrometer (CRDS) (Picarro, Inc., CA, USA, model G2401) for CO₂
 111 and CH₄ mixing ratios in the sampled air. Waiting longer would lead to unwanted mixing of the samples in the tubing.
 112 The air sample enter the tubing from the air inlet during sampling and leave the tubing from a different air outlet during
 113 later analysis. As a result, the samples at the beginning of the flight spend the same amount of time within the tubing as
 114 those at the end of the flight. Using the embedded CO₂ marker data, the CO₂ and CH₄ data series can be mapped to the
 115 sampling times and GPS locations during flight.



116
 117 **Figure 1.** Design of the air sampler.

118 2.2 The 3D sonic anemometer

119 Previous studies that applied UAV platforms for GHG monitoring generally relied wind data from nearby ground weather
 120 stations (Morales et al., 2022; Allen et al., 2019). However, Gålfalk et al. shows that wind speeds were inconsistent
 121 between a ground weather station at a 1.5 m height and an anemometer mounted on their UAV, especially when altitude
 122 increases, showing the need to have an on-board weather station for accurate flux calculations (Gålfalk et al., 2021). In
 123 the present study, in order to obtain meteorological data along the flight track, a 3D sonic anemometer (Geotech Inc,
 124 Denver, US, model Trisonica Mini) is attached on the top of the UAV via a 450 mm carbon fiber pole. The anemometer
 125 measures three-component wind speed (U_x , U_y , w) and temperature (T). The measured data were further transformed into
 126 actual wind speeds and wind directions after corrections for UAV attitude (pitch, yaw, roll) changes and accounting for
 127 its airspeed, as well as the perturbations caused by the UAV rotor propellers using a patented correction algorithm. The

128 GPS information, airspeed, and attitude data (pitch, yaw, and roll) were extracted from the UAV data transmitted to the
129 ground control station. The anemometer measures wind speeds within the range of 0 to 50 m s⁻¹, with an accuracy of ±
130 0.1 m s⁻¹ below the wind speed of 10 m s⁻¹. The accuracy for wind direction measurement is ± 1°. For temperature
131 measurement, the operating range for the anemometer is between -40 °C to 85 °C and the accuracy is ± 2 °C.

132 For anemometers mounted on multi-rotor UAVs, how to correct for the effects of the translational and rotational
133 movements of the UAVs as well as the flows induced by the rotors to obtain accurate wind data is an on-going research
134 topic (Gålfalk et al., 2021; Wolf et al., 2017; De Boisblanc et al., 2014; Palomaki et al., 2017; Zhou et al., 2018). During
135 flight, rotary wing UAVs create thrust by drawing air from above the rotors and expelling it downwards at a higher
136 velocity. Such flows may extend to the anemometer position in addition to true atmospheric air flows, masking the true
137 wind signals in the data from the anemometer (Wolf et al., 2017). Previous studies have conducted laboratory testing
138 (Wolf et al., 2017; De Boisblanc et al., 2014; Palomaki et al., 2017) or flow field simulation (Zhou et al., 2018) to
139 determine the appropriate distance to place anemometers onto multi-rotor UAVs to minimize the impact from the rotor-
140 induced air flows. The anemometer in this research is mounted at an upward distance of 70 cm from the center of gravity
141 of the UAV. A full digital model of the UAV, the anemometer and its mounting frame, and the air sampler was created.
142 Using this digital model, computational fluid dynamics (CFD) simulations were performed to quantify wind speed
143 disturbances caused by the UAV's rotor propellers on the anemometer during flight under a vast array of different wind
144 conditions. An overall correction algorithm was developed in which parameters for propeller disturbances determined
145 based on the CFD simulations were included along with correction schemes for false signals resulting from translational
146 motions and changes in UAV pitch, roll and yaw.

147 **2.3 The UAV**

148 The air sampler and the anemometer are mounted on a hexacopter UAV (KWT-X6L-15). The UAV has a maximum flight
149 time of ~30 minutes at a maximum payload of 15 kg, or longer with a lighter payload. Such flight endurance and carrying
150 capacity meet our needs for loading the air sampler and the anemometer onto the UAV to realize emission quantification.
151 The UAV is capable of flying at winds up to 14.4 m s⁻¹ to an altitude of about 4000 m and has a maximum horizontal
152 flying speed of 18 m s⁻¹, a maximum ascending speed of 4 m s⁻¹ and a maximum descending speed of 3 m s⁻¹. The
153 horizontal hovering precision of the GPS on the UAV is ± 2 m and the vertical hovering precision is ± 1.5 m.

154 **2.4 Air sample analysis**

155 After landing, the air sample collected in the tubing is immediately analyzed with the CRDS analyzer. The withdrawal
156 flow rate of the air from the sample tubing during analysis is an important parameter in optimizing the results. High
157 withdrawal rates lead to unwanted mixing in the cavity of the analyzer. However, direct withdrawal of air from the sample
158 tubing by the analyzer at a flow rate as low as the sampling flow rate of 18 sccm results in smoothing of concentrations
159 from the inner wall surface drag and desorption inside the tubing. We optimized the flow rate of the air from the sample
160 tubing into the CRDS analyzer at ~ 54 sccm, 3 times the sampling flow rate, by diluting the air sample with zero air, with
161 two mass flow controllers separately controlling the flow rate of zero air and the withdrawal rate of the air sample (Fig.
162 2b).

163 **2.5 Mass balance approaches for determining emission rates**

164 The UAV-based measurements were coupled with the mass-balance approach TERRA to determine the emission rates of
165 the measured pollutants using their measured mixing ratios and the meteorological data (three-component wind speed
166 (U_x, U_y, w) and temperature (T)) collected on board the UAV during the flight. TERRA computes integrated mass fluxes
167 through airborne virtual box/screen measurements including those made from aircraft and in this case UAVs. TERRA
168 has been used successfully and extensively for emission rate determination of tens of volatile organic compounds (Li et
169 al., 2017), CO_2 (Liggio et al., 2019), CH_4 (Baray et al., 2018), oxidized sulphur and nitrogen (Hayden et al., 2021), black
170 carbon (Cheng et al., 2020) and secondary organic aerosol (Liggio et al., 2016) using aircraft measurements. To run
171 TERRA based on a virtual box flight, the first step is to map the CH_4 and CO_2 mixing ratio data measured along the level
172 flight tracks encircling a facility to the two-dimensional virtual walls of the virtual box, created from stacking the level
173 flight tracks, that surrounds the facility. The two-dimensional virtual walls (or screens) are derived from the unwrapping
174 of the virtual box, to assist the presentation of the CH_4 and CO_2 plumes along the flight tracks, with the horizontal path
175 length (i.e., the ground line projection of the fitted flight track) and altitude as the two dimensions. The start of the
176 horizontal path is typically defined as the south-east corner of the virtual box, but the selection of this starting position
177 has no effect on the emission rate computation, and the horizontal path distance increases in a counter clockwise direction.
178 This procedure results in a translation of each flight position point from a three-dimensional position of latitude (y),
179 longitude (x), and altitude (z , above mean sea-level) to a two-dimensional screen position of horizontal path distance $s =$
180 $f(x,y)$. Subsequently, TERRA applies the Simple Kriging algorithm to interpolate the data and produces a mesh on the
181 two-dimensional virtual box walls whose resolution can be set depending on applications. The kriging weights were

182 obtained with an isotropic spherical semivariogram model. In TERRA, nugget, sill, and range can all be modified to fit
 183 the semivariogram model. The mixing ratios of both CH₄ and CO₂ are extrapolated from the lowest flight altitudes to the
 184 ground digital elevation using one of several methods or a combination thereof, namely (1) assuming a constant (2) linear
 185 extrapolation between a constant and background (3) a background value below flight altitudes (4) linear fit between the
 186 lowest flight altitude and zero at the ground and (5) exponential fit from the lower flight altitudes (Gordon et al., 2015).
 187 Concurrently measured wind speed from the UAV is decomposed into northely and easterly components
 188 ($U_N(s, z), U_E(s, z)$) based on the wind direction and similarly interpolated onto the 1 m x 2 m mesh. The decomposed
 189 wind speeds are further extrapolated to the ground digital elevation using a log profile fit (Gordon et al., 2015). Based on
 190 the interpolated/extrapolated CH₄ and CO₂ mixing ratio, temperature, pressure (calculated using barometric height
 191 formula), and wind speeds, TERRA computes the fluxes of CH₄ and CO₂ through the virtual walls and finally their facility
 192 emission rates by integrating the fluxes.

193 To summarize, in TERRA the mass-balance in computing the emissions within a control box for a given inert
 194 pollutant such as CH₄ or CO₂ is presented by:

$$195 \quad E_C = E_{C,H} + E_{C,V} - E_{C,M} , \quad (1)$$

196 where E_C is the emission rate, $E_{C,H}$ is the horizontal advective transfer rate through the box walls, $E_{C,V}$ is the advective
 197 transfer rate through the box top and $E_{C,M}$ is the increase in mass within the volume due to a change in air density. Other
 198 terms listed in the Gordon et al. computation algorithm that were used to solve for the total emission rate were often
 199 neglected as they contribute little to the total emission rates (Gordon et al., 2015). Each term from Eq. (1) is estimated as:

$$200 \quad E_{C,H} = M_R \iint X_C \rho_{air} U_{\perp} dsdz , \quad (2)$$

$$201 \quad E_{C,V} = M_R X_{C,Top} \iint \rho_{air} \omega dx dz , \quad (3)$$

$$202 \quad E_{C,M} = M_R \iiint X_C \frac{d\rho_{air}}{dt} dx dy dz , \quad (4)$$

203 where M_R is the ratio of the compound molar mass to the molar mass of air, $X_C(s, z)$ is the mixing ratio of the compound
 204 in question, $\rho_{air}(s, z)$ is the air density, w is the vertical wind velocity at the box top, $X_{C,Top}$ is the mixing ratio at the top
 205 of the box, and $U_{\perp}(s, z)$ is the horizontal normal wind vector to the flight track calculated from the northely and easterly
 206 components ($U_E(s, z), U_N(s, z)$):

$$U_{\perp}(s, z) = \frac{U_N(s, z) ds/dx - U_E(s, z) ds/dy}{\sqrt{(ds/dx)^2 + (ds/dy)^2}}, \quad (5)$$

208 The vertical transfer rate term $E_{C,V}$ is estimated by computing the air mass vertical transfer rate, determined from air
 209 mass balance within the box, and multiplying it with the CO₂ or CH₄ mixing ratios at the box top. This term is normally
 210 negligible in other top-down emission estimate approaches since it is typically miniscule compared to horizontal fluxes,
 211 but can affect the computed emission rates when vertical air movement becomes more significant such as under unstable
 212 atmospheric conditions. $E_{C,M}$ is often ignored in other mass-balance approaches; in TERRA it is estimated by taking the
 213 time derivative of the ideal gas law in temperature and pressure during the flight time, and typically it does not change
 214 significantly over the duration of 30 minutes or so for the UAV flight.

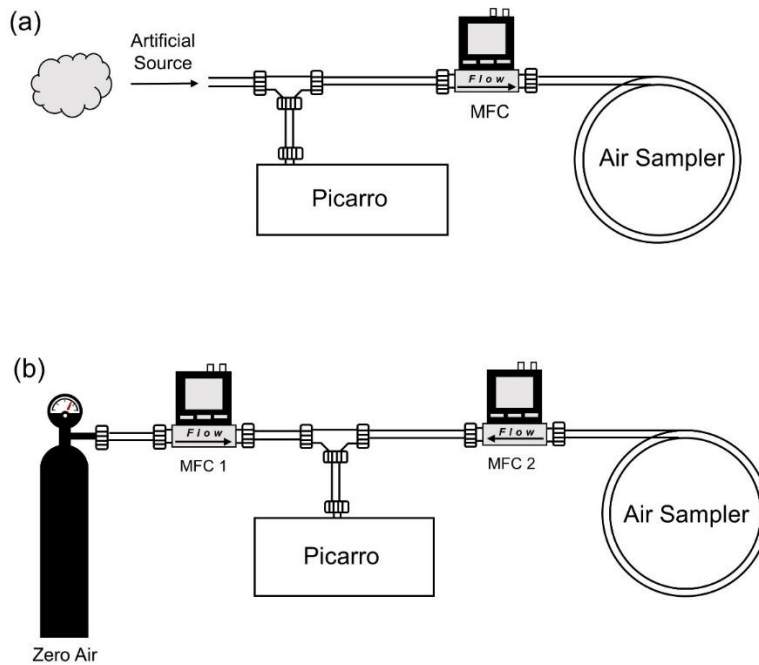
215 To suit the UAV measurements, the following modifications to the TERRA algorithm were made: (1) A much higher
 216 interpolation resolution for the kriging mesh was implemented for application to the UAV measurements in this study,
 217 with the interpolation mesh size adjusted to 1 m (vertical) by 2 m (horizontal), as UAVs fly significantly shorter distances
 218 compared to applications to piloted aircraft for which the interpolation resolution was 20 m (vertical) by 40 m (horizontal);
 219 (2) The modified TERRA now applies an embedded routine to automatically fit flight tracks using least squares, while
 220 this procedure was previously conducted manually offline through geographic information system when using TERRA.
 221 (3) The modified version of TERRA has added an algorithm for correcting negative weights during Kriging interpolation
 222 following Deutsch (Deutsch, 1995). TERRA has been updated at Peking University now recoded using the Python
 223 language and runs under a browser-server environment with a new GUI and new interactive data flow.

224 **3 Laboratory tests**

225 **3.1 Validation of the air sampler**

226 Prior to flights in the field, we validated the air sampler in laboratory experiments by first sampling an artificial air while
 227 making simultaneous online measurements of the artificial air with the CRDS analyzer, and then analyzing the sampled
 228 artificial air was with the same CRDS analyzer and comparing the results from the air sampler to the online measurements.
 229 An experimental apparatus was constructed for the simultaneous sampling of the same artificial air with the air sampler
 230 and the CRDS analyzer through a tee junction (Fig 2(a)), and subsequent air sample analysis using the same CRDS
 231 analyzer (Fig. 2(b)). In the artificial air, CH₄ and CO₂ standards were control-released into the lab air from an 8 L gas
 232 cylinder filled with a gas mixture of 5 ppm CH₄, 2 ppm CO and 600 ppm CO₂ to generate the artificial air source. The
 233 outlet of the standard gas cylinder was held at varying distances to the tee junction over time to yield a time series of

234 different CH₄ and CO₂ mixing ratios, which was designed to mimic plumes expected in the real atmosphere. During
235 analysis, the flow rate through the zero air (Mass Flow Controller 1) is adjusted to make sure that the flow rate through
236 the air sampler (Mass Flow Controller 2) is stable and consistent at 54 sccm (Sec. 2.4).



237
238 **Figure 2.** Diagram of the air sampler testing setup in the laboratory. (a) simultaneous sampling by the air sampler and the Picarro
239 CRDS analyzer. (b) subsequent air sample analysis using the picarro CRDS analyzer.

240 Figure 4(a) illustrates the mixing ratios of CO₂ and CH₄ time series obtained from the air sampler and online
241 measurements by the CRDS analyzer. It can be seen that the measured results from the air sampler and the online CRDS
242 measurements analyzer are in good agreement throughout the tests, and the correlation coefficient is estimated to be 0.89
243 and 0.73 for CH₄ and CO₂ (Fig. 4(c) and (f)). For the measurements with the air sampler, short term variations and noises
244 in the CH₄ and CO₂ mixing ratios, that were fully captured by the CRDS analyzer during the online measurements, were
245 smoothed out, while the main features and tendencies were preserved. In fact, the air sampler measurement results should
246 be a smoothed version of the CRDS analyzer online measurements, due to mixing in the analyzer cavity, molecular
247 diffusion during sample storage in the sampler, inner wall surface drag and desorption during its withdrawal from the
248 tubing during analysis, as well as Taylor dispersion during sampling and analysis (Karion et al., 2010). Dilution with zero
249 air during later CRDS analysis also contributes to the smoothing.

250 **3.2 Data deconvolution to achieve high time resolution**

251 While it is impractical to delineate the individual smoothing effects when the air sample passes through the coupled
 252 system of the sampler plus the analysis setup as described above, the measured concentration $y(t)$ can be treated as a
 253 result of the convolution of the air concentration before sampling $x(t)$ and a smoothing kernel $g(i)$ consisting of a series
 254 of weights, which are inherently determined by factors including the sampler properties (tubing length, inner diameter,
 255 temperature, absorptive properties, flow rates), storage time, dilution, and mixing in the cavity of the instrument. The
 256 smoothing can be described as:

$$257 \quad y(t) = \sum_{i=r}^s g(i)x(t-i) + n(t), t = s, s+1, \dots, n-1+r, \quad (6)$$

258 Or, expressed as a convolution of the form:

$$259 \quad y(t) = g(t) * x(t) + n(t), \quad (7a)$$

260 where $y(t)$ is the measured concentration at time t , $x(t)$ the air concentration, and $n(t)$ the unknown noise, assumed
 261 to be independent of $x(t)$. The kernel $g(i)$ contains $s-r+1$ non-zero kernel weight terms ($0 < g(i) < 1$). When all
 262 four terms in Eq. (7a) undergo Fourier transform, Eq. (7a) can be expressed in the frequency domain:

$$263 \quad Y(f) = G(f)X(f) + N(f), \quad (7b)$$

264 In order to characterize the kernel weights $g(i)$, a second lab experiment was conducted during which the sampler
 265 first sampled zero air for some time, and then sampled the CO₂ and CH₄ standards for one second, before returning to
 266 sampling zero air again, creating an original concentration pulse signal in the $x(t)$:

$$267 \quad x(t) = \begin{cases} C, & t = j \\ 0, & t \neq j \end{cases}, \quad (8)$$

268 where $j = j^{th}$ second when the sampler collected the standard of a known concentration C . This air sample was then
 269 analyzed with the CRDS as described above. After sampling, storing and analyzing, smoothing of the original
 270 concentration pulse leads to the concentration signal output $Y(t)$ as follows:

$$271 \quad y(t) = \begin{cases} \sum_{i=r}^s g(i)x(t-i) + n(t) = g(t-j)C + n(t), & t-i = j \text{ and } i = r, r+1, \dots, s \\ n(t), & t-i \neq j \end{cases}, \quad (9)$$

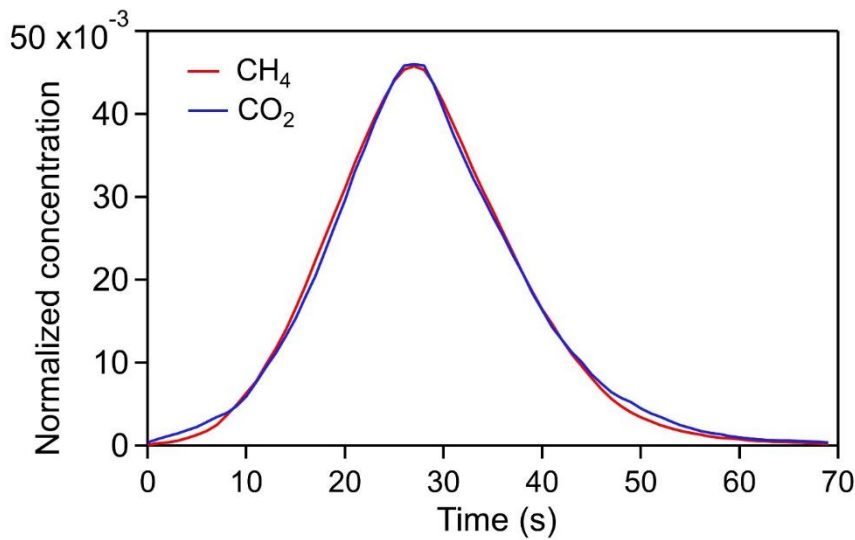
272 where $y(t)$ is the measured concentrations from the air sampler after sampling the concentration pulse and is non-zero
 273 when $t-i = j$, with the index i taking the values from r to s . The noise $n(t)$ term is zero for $t-i \neq j$ and can be
 274 assumed to have similar behavior for $t-i = j$. Therefore,

$$275 \quad g(i) = g(t-j) = \frac{1}{C}y(t) - \frac{1}{C}n(t), t = i+j \text{ and } i = r, r+1, \dots, s, \quad (10)$$

276 The second lab experiment showed that $y(t)$, and therefore the kernel $g(t)$, consists of 70 non-zero values. To remove
 277 the noise $n(t)$, $g(t)$ is further smoothed using a box-car running mean of 5 terms:

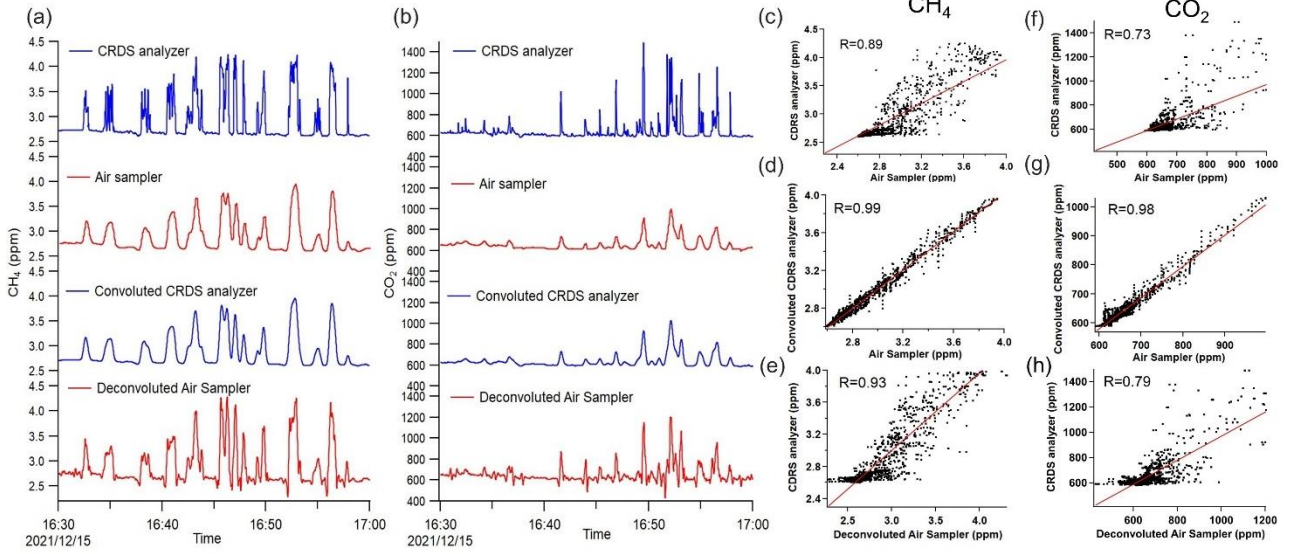
$$278 \hat{g}(t) = \frac{1}{5} \sum_{k=t-2}^{k=t+2} g(k) \approx \frac{1}{c} y(t), \quad t = i + j \text{ and } i = r, r + 1, \dots, s, \quad (11)$$

279 It could be seen from Fig. 3 that $\hat{g}(t)$ has an asymmetrical distribution with a right trailing tail and a half-height width of
 280 approximately 20 seconds for CO_2 and 21 seconds for CH_4 , indicating that the smoothing had significantly reduced the
 281 sampling/analysis method time resolution to about 20 second from the 1 second resolution of the original pulse in the air
 282 concentration. The kernel shows that the influence from the neighboring points have on a given point decreases with
 283 increases in the gap between the two points.



284
 285 **Figure 3.** The output of the one-second signal after sampling, storing and analyzing using the air sampler for CO_2 and CH_4 , normalized
 286 by their respective concentrations in the standard. As shown in the text, these curves are the actual kernel weights of $\hat{g}(t)$.

287 To test whether the kernel weights $\hat{g}(t)$ can smooth the online measured concentrations from the first lab experiment
 288 (top line in Fig. 4(a) and (b)), the weights $\hat{g}(t)$ were used to convolute with the data from the online measurements (i.e.,
 289 $x(t)$), resulting in an estimated $\hat{y}(t)$ (Fig. 4(a) and (b), third line) that is in excellent agreement with the measurements
 290 from the air sampler, with the correlation coefficients increased to 0.99 and 0.98 for CH_4 and CO_2 (Fig. 4 (d) and (g)).



291

292 **Figure 4.** (a) and (b) Mixing ratios of CO₂ and CH₄ measurements by online measurements with CRDS (the first line) and the air
 293 sampler(the second line) in laboratory tests. The third line represents the smoothed CRDS data after convolution with the kernel $\hat{g}(t)$
 294 and the fourth line represents the deconvoluted series after Wiener deconvolution. The signals of the same color represent the original
 295 signals and the corresponding signals after convolution or deconvolution (c)-(e) Correlation plots of CH₄ (f)-(h) Correlation plots of
 296 CO₂.

297 The ultimate goal of determining $\hat{g}(t)$ in Fig. 3 is to deconvolve $y(t)$ from the air sampler to obtain the original
 298 concentration series $x(t)$ using a number of deconvolution techniques. In the present study, we used the deconvolution
 299 method based on the Wiener theorem (Lin and Jin, 2013). The theorem provides the Wiener convolution filter $h(t)$ so
 300 that $x(t)$ can be estimated as follows:

$$301 \hat{x}(t) = \sum_{i=-\infty}^{\infty} h(i)y(t-i) = h(t) * y(t), \quad (12)$$

302 where $y(t)$ is the measured concentration, and $\hat{x}(t)$ an estimate of $x(t)$. In the frequency domain, Eq. (12) may be
 303 rewritten as a product of two scalars:

$$304 \hat{X}(f) = H(f)Y(f), \quad (13)$$

305 where $\hat{X}(f)$, $H(f)$, and $Y(f)$ are the Fourier transforms of $\hat{x}(t)$, $h(t)$, and $y(t)$, respectively. The Wiener convolution
 306 filter $h(t)$ is derived from the minimization of the mean square error:

$$307 \epsilon(f) = E|X(f) - \hat{X}(f)|^2, \quad (14)$$

308 with E denoting the expectation. When Eq. (7b) and Eq. (13) are substituted into Eq. (14) and the quadratic is expanded,

309 the mean square error $\epsilon(f)$ can be differentiated with respect to $H(f)$ and the derivative $\frac{d\epsilon(f)}{dH(f)}$ is set to zero to achieve

310 the minimization; under the assumption that the noise $N(f)$ is independent of $X(f)$, $H(f)$ is derived as

311
$$H(f) = \frac{G(f)S(f)}{|G(f)|^2S(f)+N(f)}, \quad (15)$$

312 where $G(f)$ is the Fourier transform of $\hat{g}(t)$ derived from the second lab experiment described above, $S(f) = E|X(f)|^2$
 313 and $N(f) = E|N(f)|^2$ are the mean power spectral densities of the original concentration series $x(t)$ and the noise $n(t)$,
 314 respectively. Equation (15) could be rewritten as:

315
$$H(f) = \frac{1}{G(f)} \left[\frac{|G(f)|^2}{|G(f)|^2+N(f)/S(f)} \right] = \frac{1}{G(f)} \left[\frac{|G(f)|^2}{|G(f)|^2+1/SNR(f)} \right], \quad (16)$$

316 where $SNR(f) = S(f)/N(f)$ is the signal-to-noise ratio.

317 Substituting Eq. (16) into Eq. (13), $\hat{X}(f)$, the Fourier transforms of $\hat{x}(t)$, is derived. The deconvolution is completed
 318 with the inverse Fourier transform of $\hat{X}(f)$ to give $\hat{x}(t)$, the estimated air concentrations. The deconvolved series of CH₄
 319 and CO₂ restored with the Wiener convolution filter are shown in Fig. 4(a) and (b), and the correlation coefficient between
 320 the deconvoluted results and the online measurements with the CRDS analyzer are 0.93 and 0.79 for CH₄ and CO₂ (Fig.
 321 4 (e) and (h)), higher than that between the original air sampler measurement and the CRDS analyzer. These results
 322 indicates the effectiveness of the Wiener theorem to deconvolve a smoothed series to a much higher time resolution while
 323 accounting for noise. The restored series is improved in terms of time resolution, from about 20 seconds mentioned above
 324 to about 3~4 seconds after the deconvolution. The lab test data from the online measurements contain strong high-
 325 frequency components, artificially manipulated to provide an extreme case for testing the deconvolution algorithm. Such
 326 high frequencies lead to some residual noise in the deconvolved results, primarily as a result of choosing the cutoff
 327 frequencies for the mean power spectral densities $S(f)$ and $N(f)$. Nevertheless, such a situation will be improved for
 328 sampling in the real atmosphere where sub-second high-frequency variations are not common.

329 **4. Field application**

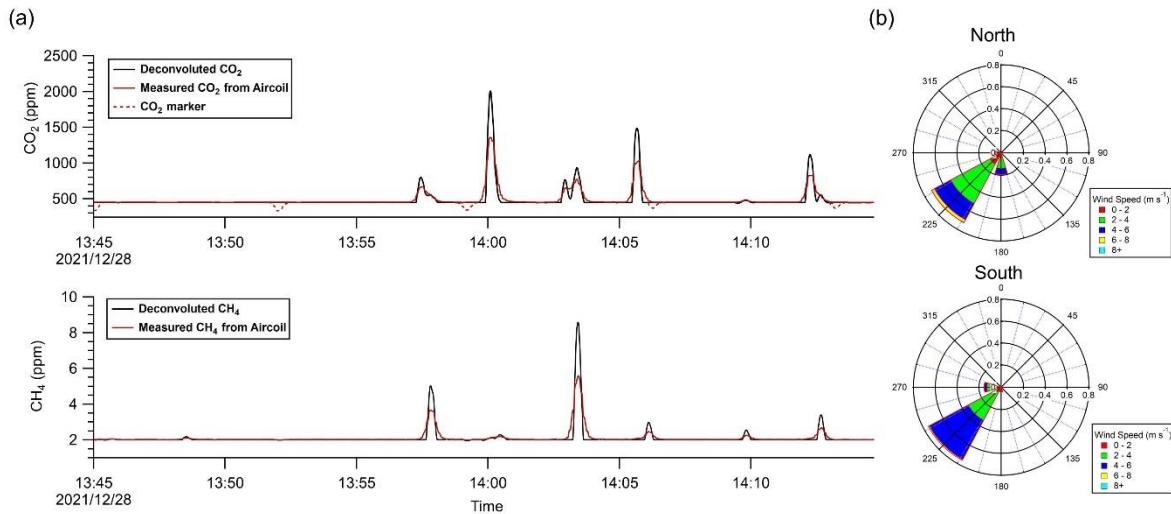
330 To apply the UAV-based measurement system described above to atmospheric measurements of CO₂ and CH₄,
 331 flights were made at the Shagang Group located in Jiangsu, China on 28 December 2021. Shagang Group is a major iron
 332 and steel company on the south shore of the Yangtze River (31.9704° N, 120.6443° E). The company produces over 40
 333 million tons of steel each year, making it one of China's top-five steel producers. Onsite coke making for iron production
 334 is located in the western part of the Shagang Steel complex. The coke making process is to dry distill coal in a coking
 335 oven at ~1000 °C temperature to boil off volatile components to form coke (metallic coal). During coke production,
 336 combustion of coking oven gas, blast furnace gas from steel making, and coal tar plus light oil for heating the coking
 337 oven is the main CO₂ and CH₄ emission source.

338 Two coking plant stacks were chosen as the target emission source for the field UAV flight. During flight, the UAV
339 was flown in a rectangle pattern (200 m×500 m) that encloses the two stacks, with repeated flight tracks at 9 altitude
340 levels that, when stacked, created a virtual box and intercepted the emitted CO₂ and CH₄ plumes on the downwind side
341 of the box. The UAV ascended from the ground to 135 m a.g.l. and started the box flight at this altitude, ascending 15 m
342 every level and reaching a maximum altitude of 255 m a.g.l. before landing. The UAV maintained a constant horizontal
343 speed of 8 m s⁻¹ during flight. The flight lasted for approximately 30 minutes. It's assumed that the plume remains steady
344 during the time of measurement. After landing, the air sample collected in the sampler was immediately analyzed with
345 the CRDS analyzer as per the procedure described above in Fig. 2(b).

346 **5. Result and discussion**

347 **5.1 CH₄ and CO₂ mixing ratio enhancement from the coking plant**

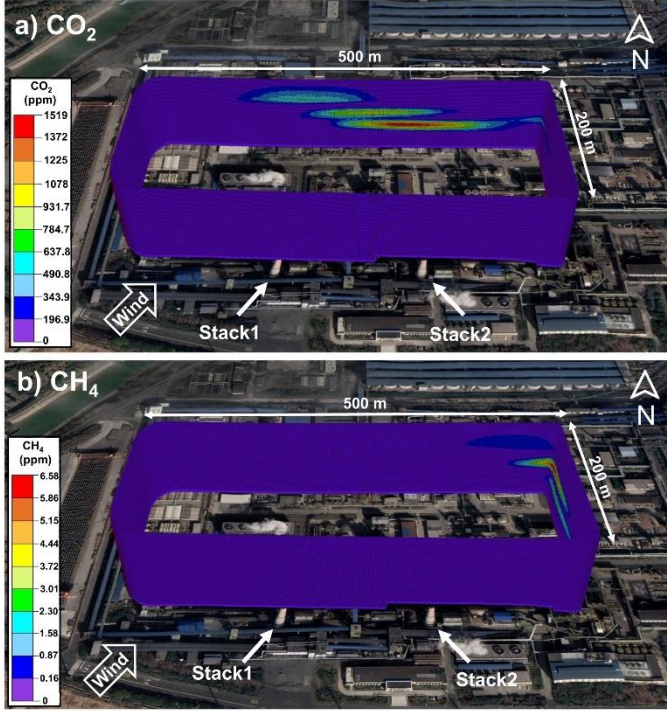
348 Figure 5(a) shows the time series of CH₄ and CO₂ mixing ratios measured with the air sampler at the coking plant during
349 the flight (red line). The air sampler sampled for a total of 30 minutes during the flight. After landing, the air sample was
350 analyzed for 10 minutes, as the analysis flow rate triples the sampling flow rate (54.0 sccm vs. 18.0 sccm). The time scales
351 of instrument readings were then stretched three times to restore the original time scales. The CH₄ and CO₂ time series
352 were then deconvolved using the convolution kernel obtained from laboratory test (Sec. 3.2) to restore the mixing ratio
353 time series in air (black line). The meteorological parameters during the time of flight were measured by the 3D
354 anemometer, showing consistent southwesterly winds (Fig. 5(b)). The average windspeed is 4.7±4.9 m s⁻¹ and the average
355 wind direction is 216.4±38.4° during the time of flight. Consistency of wind measurements can be seen from the two
356 wind rose plots for the northern wall and the southern wall respectively. During the flight, the maximum mixing ratio
357 measured was 5.6 ppm for CH₄ and 1356 ppm for CO₂. During the 30-minute flight, a total of 5 CO₂ markers were
358 generated during the 30 minutes of sampling (Fig. 5(a)), and the decreases in the marker concentrations are corrected with
359 a Gaussian form function.



360
 361 **Figure 5.** (a) Red line represents CH₄ and CO₂ mixing ratios measured from the air samples collected with the air sampler during the
 362 flight at the coking plant. Black line represents the deconvoluted CH₄ and CO₂ time series and red dashed line sections represent the
 363 original marker CO₂ concentrations every 7 minutes. (b) Wind rose plot for the northern and southern wall based on the onboard
 364 meteorological measurements during the flight.

365 5.2 Emission estimation

366 The CO₂ and CH₄ emission rates for the stacks from coking plant were estimated by applying a version of the computation
 367 algorithm TERRA specifically modified to suit UAV measurements. The deconvoluted mixing ratio time series of CO₂
 368 and CH₄ were used in the TERRA algorithm. The algorithm first maps the mixing ratios to the walls of the virtual box,
 369 then applies a kriging scheme to interpolate the data and produces a 2 m (vertical) by 1 m (horizontal) mesh on the virtual
 370 box walls (200m×500m) (Fig. 6). The semivariogram of the flight points was fitted with a spherical model (range=300,
 371 sill=3, nugget=0). Wind speed and wind direction are first decomposed into northly and easterly components, then further
 372 converted to vectors that are normal to and parallel to the walls of the virtual box before kriging. Background CH₄ and
 373 CO₂ were determined using upwind measurements. The background between upwind data was linearly interpolated and
 374 box-car smoothed within a 3-4 minute moving window to derive a variable baseline CH₄ and CO₂ for the entire 30-minute
 375 flight. As shown in Fig. 6, the CH₄ and CO₂ plumes can be seen at different locations on the downwind side of the box
 376 wall, which indicates that the CH₄ plume and the CO₂ plume probably came from different sources within the box. Using
 377 the modified version of TERRA, the emission rates for the two stacks in the coking plant were calculated to be $0.12 \pm$
 378 0.01 t h^{-1} for CH₄ and $110 \pm 20 \text{ t h}^{-1}$ for CO₂. The uncertainties for the estimates were derived from detailed analyses of
 379 each uncertainty source including measurement error in mixing ratio and wind speed, the near-surface wind extrapolation,
 380 the near-surface mixing ratio extrapolation, box-top mixing ratio, box-top height and deconvolution.



381

382 **Figure 6.** Virtual flight box for monitoring CO₂ (a) and CH₄ (b) during the flight. The CO₂ and CH₄ plumes were captured on the north
 383 and east wall respectively. The wind came from the southwestern direction. Satellite imagery © Google Earth 2019.

384 5.3 Uncertainty Analysis

385 To determine the overall uncertainty in the emission rates, each source of uncertainty contributing to the overall
 386 uncertainty needs to be identified and quantified. For the emission rate quantification from UAV measurement, the
 387 sources of uncertainties include: measurement uncertainties in the mixing ratios and wind speeds (δ_M), the near-surface
 388 wind extrapolation (δ_{Wind}), the near-surface mixing ratio extrapolation (δ_{Ex}), box-top mixing ratio (δ_{Top}), box-top height
 389 (δ_{BH}) and uncertainties due to data deconvolution as shown in the main text (δ_{Deconv}). Each uncertainty is treated as an
 390 independent estimate, and all uncertainties are propagated in quadrature to determine the overall uncertainty in the
 391 estimated emission rate:

$$392 \delta^2 = \delta_M^2 + \delta_{Wind}^2 + \delta_{Ex}^2 + \delta_{Top}^2 + \delta_{BH}^2 + \delta_{Deconv}^2, \quad (17)$$

393 The accuracy of the mixing ratio measurements from the Picarro CRDS analyzer is 50 ppb and 1 ppb for CO₂ and
 394 CH₄, respectively. By adding variations in the measured mixing ratios based on the measurement accuracies and re-
 395 applying TERRA, the derived emission rates varied within 1% for both CO₂ and CH₄. Thus, the uncertainties in the
 396 emission rates due to mixing ratio measurements (δ_M) were estimated at 1% for both CH₄ and CO₂.

397 The anemometer measures wind speeds with an accuracy of $\pm 0.1 \text{ m s}^{-1}$ at wind speeds $< 10 \text{ m s}^{-1}$ and wind directions
 398 with an accuracy of $\pm 1^\circ$. The uncertainty of the wind measurements (δ_{Wind}) was estimated using error propagation in the

399 normal wind $U_{\perp}(s, z)$, as it is calculated from the northerly and easterly wind components, thus from wind speed and
 400 wind direction:

$$401 \quad \delta_{U_{\perp}} = \sqrt{\delta_{\text{easterly}}^2 + \delta_{\text{northerly}}^2 + 2\sigma_{\text{easterly-northerly}}}, \quad (18)$$

$$402 \quad \delta_{\text{easterly}} = |\text{WSCos(WD)}\sigma_{\text{WD}}|, \quad (19)$$

$$403 \quad \delta_{\text{northerly}} = |\text{WSsin(WD)}\sigma_{\text{WD}}|, \quad (20)$$

404 Using this calculation, the uncertainty of the normal wind $\delta_{U_{\perp}}(s, z)$ was derived at each location. The uncertainty
 405 contributed to the total emission rates to the overall computed emission rate was examined by setting the normal wind to
 406 its upper and lower bounds defined by its uncertainty range, followed by computing the emission rates using TERRA.
 407 The derived CH₄ and CO₂ emission rates varied by 1.5% and 1.9% respectively. Hence the uncertainties from wind speed
 408 measurements (δ_{Wind}) were conservatively estimated to be 2% for both CH₄ and CO₂.

409 Due to a lack of near-surface measurements along the box walls, extrapolation of CH₄ and mixing ratios from the
 410 lowest flight path (~ 150 m above ground level) to the ground level has been shown to be a source of potentially large
 411 uncertainty within TERRA. The magnitude of the uncertainty depends on the nature of the emissions; for example, surface
 412 emissions which may not be fully captured by the flight altitude range have higher uncertainties at ~20%, whereas elevated
 413 stack emissions which are fully captured by flight altitude range lead to much smaller uncertainties of <4% in the emission
 414 estimates (Gordon et al., 2015). In the present study, to estimate uncertainties due to extrapolating mixing ratios from the
 415 lowest flight track to the ground (δ_{Ex}), results from all extrapolation techniques (i.e., linear to the ground, constant value
 416 to the ground, linear to background value, or some combination of methods) were derived and compared with the result
 417 using a background value below flight altitudes. Therefore, this term of uncertainty was evaluated at 2% and 6% for CH₄
 418 and CO₂ respectively.

419 **Table1.** Emission rates derived using different extrapolation techniques

Extrapolation techniques	All background below flight altitude (this study)	Constant value from lowest flight altitude to surface	Linear between constant and background at surface	linear	exponential
CH ₄ Emissions(kg h ⁻¹)	115.7	113.9	116.9	113.9	113.6
CO ₂ Emissions(kg h ⁻¹)	110100	109970	109400	109970	103960

420 Additional components contributing to uncertainties in the computed emission rates specific to the box approach
 421 include box-top mixing ratio (δ_{Top}) and box-top height (δ_{BH}). The TERRA box approach assumes a constant mixing ratio
 422 at the box top ($X_{c,Top}$) by averaging the measured value at the top level. The term δ_{Top} is determined from the 95%
 423 confidence interval ($2\sigma/\sqrt{n}$) of the interpolated measurements. The calculated confidence interval of the mixing ratio at
 424 the box top is 0.01 ± 0.13 ppm for CH₄ and 70.1 ± 89.1 ppm for CO₂. A top average mixing ratio of 0.14 ppm for CH₄
 425 and 159.2 ppm for CO₂ are set as input parameters to derive resulting uncertainties in the emissions rates. Thus, 106.6 kg
 426 h⁻¹ for CH₄ and 93760 kg h⁻¹ for CO₂ were derived. Then, this uncertainty term is conservatively taken as 8% and 16%
 427 for CH₄ and CO₂.

428 The uncertainty due to the choice of box height, δ_{BH} , within TERRA is estimated by recomputing the emission rate
 429 with a reduced box height (z) of 100 m. The recalculated emission rate after reducing the box height of 100m is 106.4 kg
 430 h⁻¹ for CH₄ and 113500 kg h⁻¹ for CO₂, thus δ_{BH} is estimated as 8% for CH₄ and 3% for CO₂.

431 For cases that use the air sampling system instead of online measuring instruments, as the CH₄ and CO₂ time series
 432 measured from the air sampler were deconvoluted to restore the unsmoothed time series before being input into the
 433 TERRA algorithm, it is necessary to account for the uncertainty that comes from such deconvolution as outlined in the
 434 main text. Time series before and after deconvolution were applied to the TERRA algorithm to obtain the total emission
 435 rates. The computations show that emission rates before and after deconvolution vary within 1%, which was taken as the
 436 uncertainty δ_{deconv} . The assessment of uncertainties for the TERRA-computed emission rates from the coking plant are
 437 listed in Table 2.

438 **Table 2.** Assessment of percent uncertainties for CH₄ and CO₂ emission rate estimations. The sources of uncertainties
 439 include: measurement uncertainties in the mixing ratios and wind speeds (δ_M), the near-surface wind extrapolation
 440 (δ_{Wind}), the near-surface mixing ratio extrapolation (δ_{Ex}), box-top mixing ratio (δ_{Top}), box-top height (δ_{BH}) and
 441 uncertainties due to data deconvolution as shown in the main text (δ_{Deconv}).

	CH ₄ (%)	CO ₂ (%)
δ_M	1	1
δ_{Wind}	2	2
δ_{Ex}	2	6
δ_{Top}	8	16
δ_{BH}	8	3
δ_{Deconv}	1	1
δ	12	18

442 5.4 Comparison with Gaussian Inversion Approach

443 The TERRA computation results can be further evaluated. Of the multiple CH₄ plumes that were captured on the north
444 and east walls of the virtual box, the largest CH₄ one resembles a nearly perfect Gaussian plume distribution and is clearly
445 associated with the east stack of the two, for which the emission rate may be recalculated using the Gaussian plume model.
446 The Gaussian plume model makes basic assumptions that the plume is emitted from a point source and that the
447 atmospheric turbulence is constant in space and time (Visscher, 2014). In this study, the captured plume was completely
448 elevated and thus not constrained by boundaries. In the absence of boundaries, the equation for pollutant mixing ratios in
449 Gaussian plumes is as follows:

$$450 \quad c = \frac{Q}{2\pi\bar{u}\sigma_y\sigma_z} \exp\left(-\frac{y^2}{2\sigma_y^2}\right) \exp\left(-\frac{(z-h)^2}{2\sigma_z^2}\right), \quad (21)$$

451 where c is the concentration at a given position x , y and z (g m^{-3}), Q is the emission rate (g s^{-1}), \bar{u} is the mean wind speed
452 (m s^{-1}), h is the effective source height (m) and σ_y and σ_z are dispersion parameters in the horizontal (lateral) and vertical
453 directions respectively (m).

454 The dispersion parameters σ_y and σ_z were obtained by fitting the spatial distribution of CH₄ mixing ratios on the
455 measurement screen into a Gaussian function. As the wall intercepting the plume is not perpendicular to the wind direction,
456 the plume was projected to a different virtual wall perpendicular to the wind direction before fitting the Gaussian function.
457 By calculating the standard deviations of the Gaussian distributions in the y and z directions, σ_z is estimated to be $6.3 \pm$
458 0.3 m and σ_y is 15.7 ± 0.4 m. The downwind measurement plane is examined to find the point with the highest CH₄
459 mixing ratio of 6.575 ppm and its location ($s = 160$ m, $z = 217$ m). For the separate CH₄ plume, the Gaussian plume model
460 gives an emission rate of 40 ± 6.8 kg h⁻¹. The uncertainty is quantified by considering the accuracy of mixing ratio
461 measurement, the variation of wind speed and the confidence interval for the dispersion parameters given by Gaussian
462 function fitting. CH₄ measurement uncertainties from the instrument is <1%. The uncertainty contributed by the mean
463 wind speed estimation was examined by varying the average wind speed by the standard deviation of the wind data around
464 the plume (3.8 ± 0.6 m s⁻¹), followed by input into gaussian plume model. This mean wind speed sensitivity analysis
465 resulted in CH₄ emission rates that varied by 16%. The same sensitivity analysis was done with σ_y (15.7 ± 0.4 m) and σ_z
466 (6.3 ± 0.3 m), which resulted in CH₄ emission rates that varied by 4% and 3% respectively. Thus, the total uncertainty is
467 added in quadrature to be 17%. The TERRA algorithm is able to obtain the emission rate for a selected section through a
468 certain area of the screen. For this isolated CH₄ plume, the TERRA algorithm computed an emission rate of 65 ± 8 kg h⁻¹,
469 which is comparable to the emission rate estimation from the Gaussian plume model.

470 5.5 Validation of UAV-based Emissions and Comparison with IPCC-based Emissions

471 Coking process is one of the highest energy-consuming operations during iron and steel production that tends to emit
472 large amounts of CO₂ and CH₄. According to the Chinese national GHG inventory report, CO₂ and CH₄ emissions from
473 coke production in iron and steel production processes were calculated using the Tier 1 method in the IPCC Guidelines
474 (Ministry of Ecology and Environment of of China, 2018). In the Tier 1 method, default emission factors for coke
475 production are used to estimate the CO₂ and CH₄ emissions without considering local variations, respectively,

$$476 E_{\text{CO}_2} = P_{\text{coke}} \times EF_{\text{CO}_2} \text{ and } E_{\text{CH}_4} = P_{\text{coke}} \times EF_{\text{CH}_4}, \quad (22)$$

477 where E_{CO_2} and E_{CH_4} represents the CO₂ and CH₄ emission rates from coke production, P_{coke} represents coke production,
478 EF_{CO_2} and EF_{CH_4} are the IPCC default emission factors for CO₂ and CH₄, which are 0.56 t CO₂/t of coke and 0.1 g CH₄/t
479 of coke, respectively. The measured Shagang coking plant consists of two coke oven batteries, each with its own stack.
480 Each battery produced 127.8 t coke h⁻¹, thus totalling 255.6 t coke h⁻¹ (P_{coke}) between the two batteries during the UAV
481 measurement period with a coke yield of 78.5%. A material balance analysis revealed that CO₂ emitted from the stacks
482 during the full coking process was 103±32 t CO₂ h⁻¹ (SI). In comparison, the UAV measurement-based emission rate
483 obtained in this study is 110±18 t CO₂ h⁻¹, which is consistent with the CO₂ emissions based on the material balance
484 analysis. For comparison, multiplying the IPCC default emission factor with the coke production at the Shagang coking
485 plant yields an emission rate from coking of 143 t CO₂ h⁻¹, higher than either the material balance based result by about
486 39% or the UAV-based result by 30%. This suggests that the IPCC default emission factor is too high for this particular
487 coking plant.

488 On the other hand, the UAV-measurement based emission of 0.12±0.014 t h⁻¹ for CH₄ is four orders of magnitude
489 higher than 1.28×10⁻⁵ t h⁻¹ emissions for CH₄ estimated using the IPCC Tier 1 emission factor EF_{CH_4} . The IPCC emission
490 factor for coke production is derived by averaging plant-specific CH₄ emissions data for 11 European coke plants reported
491 in the IPPC I&S BAT Document (European IPPC Bureau, 2001), but information about the data collection method such
492 as sampling methods, analysis methods, time intervals, computation methods and reference conditions is not available
493 according the report. It is important to note that the present UAV measurement represents a one-time measurement where
494 there was only one flight conducted in this campaign. The result clearly serves the purpose for validating the overall
495 methodology from air sampling and analysis, computing the emission rates, to estimating the associated errors. The
496 fundamental assumption in the mass balance approach is that plumes and emissions remain constant throughout the
497 measurement period. Given the short duration of the flight and the good comparison between the present emission result
498 and the material balance emission estimate, such an assumption appears to be valid. However, a hypothesis of a constant

499 emission rate over time remains to be tested. Conducting multiple flights over time, computing emission rates and
500 assessing their uncertainties will allow for statistical sampling of the probability distribution of the emission rates and
501 hence deriving the mathematical expectation of the emission rate. Only then the derived emission factors can be used for
502 inventory preparation and/or comparison with existing ones with statistical confidence. Given the limited circumstance
503 of having only one flight in this study, it becomes clear such purpose cannot be achieved. Consequently, the emission
504 values of CH₄ derived from measurements in this section are only suitable for qualitative comparisons with published
505 emission factors. The comparison results indicate that real-world emission factors may significantly differ from the default
506 emission factors but more work is needed. The additional CH₄ may come from the leakage of the coke oven gas when it
507 is recycled as fuel in firing the coke oven (SI). Both reasons point to a need for further emission measurements to
508 determine the local emission factors and a further validation of the CH₄ emission factors of coke production.

509 **6 Conclusions**

510 In this paper, we present the development of a UAV measurement system for quantifying GHG emissions at facility levels.
511 The key element of this system is a newly designed air sampler, consisting of a 150-meter-long thin-walled stainless steel
512 tube with remote-controlled time stamping. Through laboratory testing, we found that the air sampler generated smoothed
513 time series data compared to online measurement by the CRDS analyzer. To addressing the smoothing effect, we
514 developed a deconvolution algorithm to restore the resolution of the time series obtained by the air sampler. For field
515 validation, the new UAV measurement system was deployed at the Shagang Steel to obtain CO₂ and CH₄ emissions from
516 the main coking plant at Shagang Steel. Mixing ratios of CO₂ and CH₄ together with meteorological parameters were
517 measured during the test flight. The mass-balance algorithm TERRA was used to estimate the coking plant CO₂ and CH₄
518 emission rates based on the UAV-measured data. For further analysis, we compared these emission results with those
519 derived using Gaussian plume inversion approach and carbon material balance methods, demonstrating good consistency
520 among different approaches. In addition, when compared the top-down UAV-based measurement results to that derived
521 from the bottom-up emission inventory method, the present findings indicated that the IPCC emission factors can be
522 significantly different from the actual emission factors..

523 *Acknowledgment.* This project was supported by a grant from the National Natural Science Foundation of China Creative
524 Research Group Fund (22221004).

525 *Data availability.* Data are available upon request by the corresponding author.

526 *Author contribution.* TH, CX, YL and, SML conducted the fieldwork with the support by XG, XZ, and FB. TH and CX
527 conducted laboratory experiments with the guidance by SML. TH performed the primary data analysis, and wrote the
528 initial draft of the manuscript. YH provided expertise in model analysis. Algorithm programming was provided by YL.
529 YY and YZ did the wind data correction. SML reviewed and edited the manuscript, and ensured the accuracy and integrity
530 of the study.

531 *Competing interests.* The authors declare that they have no conflict of interest.

532 **Reference**

- 533 Allen, G., Hollingsworth, P., Kabbabe, K., Pitt, J. R., Mead, M. I., Illingworth, S., Roberts, G., Bourn, M., Shallcross, D.
534 E., and Percival, C. J.: The development and trial of an unmanned aerial system for the measurement of methane
535 flux from landfill and greenhouse gas emission hotspots, *Waste Management*, 87, 883-892,
536 doi:10.1016/j.wasman.2017.12.024, 2019.
- 537 Andersen, T., Scheeren, B., Peters, W., and Chen, H.: A UAV-based active AirCore system for measurements of
538 greenhouse gases, *Atmos. Meas. Tech.*, 11, 2683-2699, doi:10.5194/amt-11-2683-2018, 2018.
- 539 Andersen, T., Vinkovic, K., de Vries, M., Kers, B., Necki, J., Swolkien, J., Roiger, A., Peters, W., and Chen, H.:
540 Quantifying methane emissions from coal mining ventilation shafts using an unmanned aerial vehicle (UAV)-based
541 active AirCore system, *Atmos. Environ.*, X, 12, doi:10.1016/j.aeaoa.2021.100135, 2021.
- 542 Angeli, S. D., Gossler, S., Lichtenberg, S., Kass, G., Agrawal, A. K., Valerius, M., Kinzel, K. P., and Deutschmann, O.:
543 Reduction of CO₂ emission from off-gases of steel industry by dry reforming of methane, *Angew. Chem. Int. Ed.*,
544 60, 11852-11857, doi:10.1002/anie.202100577, 2021.
- 545 Baray, S., Darlington, A., Gordon, M., Hayden, K. L., Leithead, A., Li, S.-M., Liu, P. S. K., Mittermeier, R. L., Moussa,
546 S. G., O'Brien, J., Staebler, R., Wolde, M., Worthy, D., and McLaren, R.: Quantification of methane sources in the
547 Athabasca Oil Sands Region of Alberta by aircraft mass balance, *Atmos. Chem. Phys.*, 18, 7361-7378,
548 doi:10.5194/acp-18-7361-2018, 2018.
- 549 Bel Hadj Ali, N., Abichou, T., and Green, R.: Comparing estimates of fugitive landfill methane emissions using inverse
550 plume modeling obtained with Surface Emission Monitoring (SEM), Drone Emission Monitoring (DEM), and

551 Downwind Plume Emission Monitoring (DWPEM), *J. Air Waste Manage. Assoc.*, 70, 410-424,
552 doi:10.1080/10962247.2020.1728423, 2020.

553 Brantley, H. L., Thoma, E. D., Squier, W. C., Guven, B. B., and Lyon, D.: Assessment of methane emissions from oil
554 and gas production pads using mobile measurements, *Environ. Sci. Technol.*, 48, 14508-14515,
555 doi:10.1021/es503070q, 2014.

556 Brownlow, R., Lowry, D., Thomas, R. M., Fisher, R. E., France, J. L., Cain, M., Richardson, T. S., Greatwood, C., Freer,
557 J., Pyle, J. A., MacKenzie, A. R., and Nisbet, E. G.: Methane mole fraction and $\delta^{13}\text{C}$ above and below the trade
558 wind inversion at Ascension Island in air sampled by aerial robotics, *Geophys. Res. Lett.*, 43,
559 doi:10.1002/2016gl071155, 2016.

560 Chang, C. C., Wang, J. L., Chang, C. Y., Liang, M. C., and Lin, M. R.: Development of a multicopter-carried whole air
561 sampling apparatus and its applications in environmental studies, *Chemosphere*, 144, 484-492,
562 doi:10.1016/j.chemosphere.2015.08.028, 2016.

563 Cheng, Y., Li, S. M., Liggio, J., Gordon, M., Darlington, A., Zheng, Q., Moran, M., Liu, P., and Wolde, M.: Top-Down
564 Determination of Black Carbon Emissions from Oil Sand Facilities in Alberta, Canada Using Aircraft Measurements,
565 *Environ. Sci. Technol.*, 54, 412-418, doi:10.1021/acs.est.9b05522, 2020.

566 Chiba, T.; Haga, Y.; Inoue, M.; Kiguchi, O.; Nagayoshi, T.; Madokoro, H.; Morino, I.: Measuring Regional Atmospheric
567 CO_2 Concentrations in the Lower Troposphere with a Non-Dispersive Infrared Analyzer Mounted on a UAV, Ogata
568 Village, Akita, Japan, *Atmosphere*, 10, 487, doi:10.3390/atmos10090487, 2019.

569 De Boisblanc, I., Dodbele, N., Kussmann, L., Mukherji, R., Chestnut, D., Phelps, S., Lewin, G. C., and de Wekker, S.:
570 Designing a hexacopter for the collection of atmospheric flow data, 2014 Systems and Information Engineering
571 Design Symposium (SIEDS), 147-152, doi:10.1109/SIEDS.2014.6829915, 2014.

572 Deutsch, C. V.: Correcting for negative weights in ordinary kriging, *Comput. Geosc.*, 22(7), 765-773, doi:10.1016/0098-
573 3004(96)00005-2, 1996.

574 Etminan, M., Myhre, G., Highwood, E., and Shine, K.: Radiative forcing of carbon dioxide, methane, and nitrous oxide:
575 A significant revision of the methane radiative forcing, *Geophys. Res. Lett.*, 43, 12,614-612,623,
576 doi:10.1002/2016GL071930, 2016.

577 European IPPC Bureau, Integrated Pollution Prevention and Control (IPPC) Best Available Techniques Reference
578 Document on the Production of Iron and Steel, 2001.

579 Gålfalk, M., Nilsson Paledal, S., and Bastviken, D.: Sensitive Drone Mapping of Methane Emissions without the Need
580 for Supplementary Ground-Based Measurements, *ACS Earth Space Chem.*, 5, 2668-2676,
581 doi:10.1021/acsearthspacechem.1c00106, 2021.

582 Golston, L., Aubut, N., Frish, M., Yang, S., Talbot, R., Gretencord, C., McSpirt, J., and Zondlo, M.: Natural Gas Fugitive
583 Leak Detection Using an Unmanned Aerial Vehicle: Localization and Quantification of Emission Rate, *Atmosphere*,
584 9, doi:10.3390/atmos9090333, 2018.

585 Gordon, M., Li, S. M., Staebler, R., Darlington, A., Hayden, K., O'Brien, J., and Wolde, M.: Determining air pollutant
586 emission rates based on mass balance using airborne measurement data over the Alberta oil sands operations, *Atmos.*
587 *Meas. Tech.*, 8, 3745-3765, doi:10.5194/amt-8-3745-2015, 2015.

588 Hasanbeigi, A.: *Steel Climate Impact - An International Benchmarking of Energy and CO2 Intensities*, Global Efficiency
589 Intelligence, Florida, United States, 2022.

590 Hayden, K., Li, S.-M., Makar, P., Liggio, J., Moussa, S. G., Akingunola, A., McLaren, R., Staebler, R. M., Darlington,
591 A., O'Brien, J., Zhang, J., Wolde, M., and Zhang, L.: New methodology shows short atmospheric lifetimes of
592 oxidized sulfur and nitrogen due to dry deposition, *Atmos. Chem. Phys.*, 21, 8377-8392, doi:10.5194/acp-21-8377-
593 2021, 2021.

594 Helfter, C., Tremper, A. H., Halios, C. H., Kotthaus, S., Bjorkegren, A., Grimmond, C. S. B., Barlow, J. F., and Nemitz,
595 E.: Spatial and temporal variability of urban fluxes of methane, carbon monoxide and carbon dioxide above London,
596 UK, *Atmos. Chem. Phys.*, 16, 10543-10557, doi:10.5194/acp-16-10543-2016, 2016.

597 IPCC, 2006 IPCC Guidelines for National Greenhouse Gas Inventories, Chapter 4: Metal Industry Emissions, 2016.

598 IPCC, 2021: *Climate Change 2021: The Physical Science Basis. Contribution of Working Group I to the Sixth Assessment*
599 *Report of the Intergovernmental Panel on Climate Change*[Masson-Delmotte, V., P. Zhai, A. Pirani, S.L. Connors,
600 C. Péan, S. Berger, N. Caud, Y. Chen, L. Goldfarb, M.I. Gomis, M. Huang, K. Leitzell, E. Lonnoy, J.B.R. Matthews,
601 T.K. Maycock, T. Waterfield, O. Yelekçi, R. Yu, and B. Zhou (eds.)]. Cambridge University Press, Cambridge,
602 United Kingdom and New York, NY, USA, 2391 pp. doi:10.1017/9781009157896.

603 Karion, A., Sweeney, C., Tans, P., and Newberger, T.: AirCore: An innovative atmospheric sampling system, *J. Atmo.*
604 *Ocean. Technol.*, 27, 1839-1853, doi:10.1175/2010JTECHA1448.1, 2010.

605 Leitner, S., Feichtinger, W., Mayer, S., Mayer, F., Krompetz, D., Hood-Nowotny, R., and Watzinger, A.: UAV-based
606 sampling systems to analyse greenhouse gases and volatile organic compounds encompassing compound-specific
607 stable isotope analysis, *Atmos. Meas. Tech.*, 16, 513–527, doi:10.5194/amt-16-513-2023, 2023.

608 Li, H. Z., Mundia-Howe, M., Reeder, M. D., and Pekney, N. J.: Gathering Pipeline Methane Emissions in Utica Shale
609 Using an Unmanned Aerial Vehicle and Ground-Based Mobile Sampling, *Atmosphere*, 11,
610 doi:10.3390/atmos11070716, 2020.

611 Li, S. M., Leithead, A., Moussa, S. G., Liggio, J., Moran, M. D., Wang, D., Hayden, K., Darlington, A., Gordon, M.,
612 Staebler, R., Makar, P. A., Stroud, C. A., McLaren, R., Liu, P. S. K., O'Brien, J., Mittermeier, R. L., Zhang, J.,
613 Marson, G., Cober, S. G., Wolde, M., and Wentzell, J. J. B.: Differences between measured and reported volatile
614 organic compound emissions from oil sands facilities in Alberta, Canada, *Proc. Natl. Acad. Sci. U. S. A.*, 114, E3756-
615 E3765, doi:10.1073/pnas.1617862114, 2017.

616 Liggio, J., Li, S. M., Hayden, K., Taha, Y. M., Stroud, C., Darlington, A., Drollette, B. D., Gordon, M., Lee, P., Liu, P.,
617 Leithead, A., Moussa, S. G., Wang, D., O'Brien, J., Mittermeier, R. L., Brook, J. R., Lu, G., Staebler, R. M., Han,
618 Y., Tokarek, T. W., Osthoff, H. D., Makar, P. A., Zhang, J., Plata, D. L., and Gentner, D. R.: Oil sands operations
619 as a large source of secondary organic aerosols, *Nature*, 534, 91-94, doi:10.1038/nature17646, 2016.

620 Liggio, J., Li, S. M., Staebler, R. M., Hayden, K., Darlington, A., Mittermeier, R. L., O'Brien, J., McLaren, R., Wolde,
621 M., Worthy, D., and Vogel, F.: Measured Canadian oil sands CO₂ emissions are higher than estimates made using
622 internationally recommended methods, *Nat. Commun.*, 10, 1863, doi:10.1038/s41467-019-09714-9, 2019.

623 Lin, F. and Jin, C.: An improved Wiener deconvolution filter for high-resolution electron microscopy images, *Micron*,
624 50, 1-6, doi:10.1016/j.micron.2013.03.005, 2013.

625 Liu, Y., Paris, J.-D., Vrekoussis, M., Antoniou, P., Constantinides, C., Desservettaz, M., Keleshis, C., Laurent, O.,
626 Leonidou, A., Philippon, C., Vouterakos, P., Quéhé, P.-Y., Bousquet, P., and Sciare, J.: Improvements of a low-cost
627 CO₂ commercial nondispersive near-infrared (NDIR) sensor for unmanned aerial vehicle (UAV) atmospheric
628 mapping applications, *Atmos. Meas. Tech.*, 15, 4431–4442, doi:10.5194/amt-15-4431-2022, 2022.

629 Miller, S. M., Wofsy, S. C., Michalak, A. M., Kort, E. A., Andrews, A. E., Biraud, S. C., Dlugokencky, E. J., Eluszkiewicz,
630 J., Fischer, M. L., Janssens-Maenhout, G., Miller, B. R., Miller, J. B., Montzka, S. A., Nehrkorn, T., and Sweeney,
631 C.: Anthropogenic emissions of methane in the United States, *Proc. Natl. Acad. Sci. U. S. A.*, 110, 20018-20022,
632 doi:10.1073/pnas.1314392110, 2013.

633 Ministry of Ecology and Environment of China, The People's Republic of China Second Biennial Update Report on
634 Climate Change, Part II National Greenhouse Gas Inventory, Chapter 1.3 Industrial Process, 2018.

635 Morales, R., Ravelid, J., Vinkovic, K., Korbeń, P., Tuzson, B., Emmenegger, L., Chen, H., Schmidt, M., Humbel, S., and
636 Brunner, D.: Controlled-release experiment to investigate uncertainties in UAV-based emission quantification for
637 methane point sources, *Atmos. Meas. Tech.*, 15, 2177-2198, doi:10.5194/amt-15-2177-2022, 2022.

638 Nathan, B. J., Golston, L. M., O'Brien, A. S., Ross, K., Harrison, W. A., Tao, L., Lary, D. J., Johnson, D. R., Covington,
639 A. N., Clark, N. N., and Zondlo, M. A.: Near-Field Characterization of Methane Emission Variability from a
640 Compressor Station Using a Model Aircraft, *Environ. Sci. Technol.*, 49, 7896-7903, doi:10.1021/acs.est.5b00705,
641 2015.

642 Palomaki, R. T., Rose, N. T., van den Bossche, M., Sherman, T. J., and De Wekker, S. F. J.: Wind Estimation in the
643 Lower Atmosphere Using Multicopter Aircraft, *J. Atmos. Ocean. Technol.*, 34, 1183-1191, doi:10.1175/jtech-d-16-
644 0177.1, 2017.

645 Rella, C. W., Tsai, T. R., Botkin, C. G., Crosson, E. R., and Steele, D.: Measuring emissions from oil and natural gas well
646 pads using the mobile flux plane technique, *Environ. Sci. Technol.*, 49, 4742-4748, doi:10.1021/acs.est.5b00099,
647 2015.

648 Saunio, M., Stavert, A. R., Poulter, B., Bousquet, P., Canadell, J. G., Jackson, R. B., Raymond, P. A., Dlugokencky, E.
649 J., Houweling, S., Patra, P. K., Ciais, P., Arora, V. K., Bastviken, D., Bergamaschi, P., Blake, D. R., Brailsford, G.,
650 Bruhwiler, L., Carlson, K. M., Carrol, M., Castaldi, S., Chandra, N., Crevoisier, C., Crill, P. M., Covey, K., Curry,
651 C. L., Etiope, G., Frankenberg, C., Gedney, N., Hegglin, M. I., Höglund-Isaksson, L., Hugelius, G., Ishizawa, M.,
652 Ito, A., Janssens-Maenhout, G., Jensen, K. M., Joos, F., Kleinen, T., Krummel, P. B., Langenfelds, R. L., Laruelle,
653 G. G., Liu, L., Machida, T., Maksyutov, S., McDonald, K. C., McNorton, J., Miller, P. A., Melton, J. R., Morino, I.,
654 Müller, J., Murguía-Flores, F., Naik, V., Niwa, Y., Noce, S., O'Doherty, S., Parker, R. J., Peng, C., Peng, S., Peters,
655 G. P., Prigent, C., Prinn, R., Ramonet, M., Regnier, P., Riley, W. J., Rosentreter, J. A., Segers, A., Simpson, I. J.,
656 Shi, H., Smith, S. J., Steele, L. P., Thornton, B. F., Tian, H., Tohjima, Y., Tubiello, F. N., Tsuruta, A., Viovy, N.,
657 Voulgarakis, A., Weber, T. S., van Weele, M., van der Werf, G. R., Weiss, R. F., Worthy, D., Wunch, D., Yin, Y.,
658 Yoshida, Y., Zhang, W., Zhang, Z., Zhao, Y., Zheng, B., Zhu, Q., Zhu, Q., and Zhuang, Q.: The Global Methane
659 Budget 2000–2017, *Earth Syst. Sci. Data*, 12, 1561-1623, doi:10.5194/essd-12-1561-2020, 2020.

660 Reuter, M., Bovensmann, H., Buchwitz, M., Borchardt, J., Krautwurst, S., Gerilowski, K., Lindauer, M., Kubistin, D.,
661 and Burrows, J. P.: Development of a small unmanned aircraft system to derive CO₂ emissions of anthropogenic
662 point sources, *Atmos. Meas. Tech.*, 14, 153–172, doi:10.5194/amt-14-153-2021, 2021.

663 Shah, A., Ricketts, H., Pitt, J. R., Shaw, J. T., Kabbabe, K., Leen, J. B., and Allen, G.: Unmanned aerial vehicle
664 observations of cold venting from exploratory hydraulic fracturing in the United Kingdom, *Environ. Res. Commun.*,
665 2, 021003, doi:10.1088/2515-7620/ab716d, 2020.

666 Shaw, J. T., Shah, A., Yong, H., and Allen, G.: Methods for quantifying methane emissions using unmanned aerial
667 vehicles: a review, *Philos. Trans. Royal Soc. A*, 379, 20200450, doi:10.1098/rsta.2020.0450, 2021.

668 Takano, T. and Ueyama, M.: Spatial variations in daytime methane and carbon dioxide emissions in two urban landscapes,
669 Sakai, Japan, *Urban Clim.*, 36, 100798, doi:10.1016/j.uclim.2021.100798, 2021.

670 Turner, A. J., Jacob, D. J., Wecht, K. J., Maasackers, J. D., Lundgren, E., Andrews, A. E., Biraud, S. C., Boesch, H.,
671 Bowman, K. W., Deutscher, N. M., Dubey, M. K., Griffith, D. W. T., Hase, F., Kuze, A., Notholt, J., Ohyama, H.,
672 Parker, R., Payne, V. H., Sussmann, R., Sweeney, C., Velazco, V. A., Warneke, T., Wennberg, P. O., and Wunch,
673 D.: Estimating global and North American methane emissions with high spatial resolution using GOSAT satellite
674 data, *Atmos. Chem. Phys.*, 15, 7049-7069, doi:10.5194/acp-15-7049-2015, 2015.

675 Turner, A. J., Frankenberg, C., and Kort, E. A.: Interpreting contemporary trends in atmospheric methane, *Proc. Natl.*
676 *Acad. Sci. U. S. A.*, 116, 2805-2813, 10.1073/pnas.1814297116, 2019.

677 Tuzson, B., Morales, R., Graf, M., Scheidegger, P., Looser, H., Kupferschmid, A., and Emmenegger, L.: Bird's-eye View
678 of Localized Methane Emission Sources: Highlights of Analytical Sciences in Switzerland, *Chimia*, 75, 802-802,
679 doi:10.2533/chimia.2021.802, 2021.

680 U.S. Environmental Protection Agency, *Inventory of U.S. Greenhouse Gas Emissions and Sinks: 1990 – 2014*, 2016.

681 Vinkovic, K., Andersen, T., de Vries, M., Kers, B., van Heuven, S., Peters, W., Hensen, A., van den Bulk, P., and Chen,
682 H.: Evaluating the use of an Unmanned Aerial Vehicle (UAV)-based active AirCore system to quantify methane
683 emissions from dairy cows, *Sci. Total. Environ.*, 831, 154898, doi:10.1016/j.scitotenv.2022.154898, 2022.

684 Visscher, A. D.: *Air Dispersion Modeling: Foundations and Applications*, John Wiley & Sons, Inc., Hoboken, New Jersey,
685 2014.

686 Wolf, C. A., Hardis, R. P., Woodrum, S. D., Galan, R. S., Wichelt, H. S., Metzger, M. C., Bezzo, N., Lewin, G. C., and
687 de Wekker, S. F.: Wind data collection techniques on a multi-rotor platform, 2017 *Systems and Information*
688 *Engineering Design Symposium (SIEDS)*, 32-37, doi:10.1109/SIEDS.2017.7937739, 2017.

689 Zhou, S., Peng, S., Wang, M., Shen, A., and Liu, Z.: The Characteristics and Contributing Factors of Air Pollution in
690 Nanjing: A Case Study Based on an Unmanned Aerial Vehicle Experiment and Multiple Datasets, *Atmosphere*, 9,
691 doi:10.3390/atmos9090343, 2018.